Journal of Materials Chemistry C

ROYAL SOCIETY OF CHEMISTRY

PAPER

View Article Online
View Journal | View Issue

Cite this: *J. Mater. Chem. C*, 2021, **9**, 13226

Discovery of high performance thermoelectric chalcogenides through first-principles high-throughput screening†

Tao Fan * and Artem R. Oganov

Received 6th July 2021,
Accepted 12th August 2021

DOI: 10.1039/d1tc03146e

rsc.li/materials-c

Searching for thermoelectric materials with high energy conversion efficiency is important to solve the energy and environment issues of our society. In this work, we studied the thermoelectric and related transport properties of 127 cubic chalcogenides using first-principles methods. Specifically, the electrical transport properties were computed based on the generalized Kane band model and perturbation theory under the relaxation time approximation for charge carriers, which is fast and relatively accurate. The dependence of power factor on temperature and carrier concentration was investigated. There are 46 compounds showing that their maximum power factors could be larger than 10 μW cm^{-1} K^{-2} if fully optimized. Furthermore, lattice thermal conductivities were calculated based on a modified Debye–Callaway model and thermoelectric figure of merit *ZT* was obtained. 19 compounds were found to potentially have *ZT* greater than 1 for either n-type or p-type transport. Several compounds with excellent performance are recommended as potentially good thermoelectric materials based on our calculations.

1 Introduction

Thermoelectric materials, which can convert heat to electricity and *vice versa*, could play an important role in improving energy consumption efficiency and building clean and alternative energy sources.[1–4] Advanced thermoelectric generators could increase the production of electricity from solar, co-generation and waste heat sources. Improved solid-state thermoelectric refrigerators could replace compression-based refrigeration systems, providing thermal management solutions at both small and building scales.[5,6] The performance of a thermoelectric material at a given temperature T is quantified by its dimensionless figure of merit (ZT). ZT is defined as $ZT = \alpha^2\sigma T/(\kappa_e + \kappa_L)$, where α is the Seebeck coefficient, σ is the electrical conductivity, κ_e is the electronic thermal conductivity, and κ_L is the lattice thermal conductivity. Particularly, $\alpha^2\sigma$ is called the power factor (PF). In order to obtain a high ZT, both α and σ must be maximized, while κ_e and κ_L need to be minimized. However, the interdependence of these parameters makes it challenging to improve the ZT of a material.[7–9]

With the advance of theory and increase of computing power, materials research and discovery based on first-principles methods are becoming popular. This approach has been used in many research fields and led to interesting discoveries.[10–12] The first high-throughput search for thermoelectric materials was done by Madsen based on semi-classical Boltzmann transport theory with constant relaxation time approximation (CRTA), as implemented in BoltzTrap.[13,14] In that work, transport properties of 570 Sb-containing compounds were assessed and LiZnSb was identified as a promising n-type candidate. Later, Yang *et al.* used the same method to study 36 half-Heusler (HH) compounds. The calculated maximum power factors suggested Co-, Rh- and Fe-based HHs as p-type, and LaPdBi as n-type prospective materials.[15] Zhu *et al.* used the same method to screen ~9000 materials based on the Materials Project database.[16,17] They identified trigonal and tetragonal $TmAgTe_2$ as potential candidates with ZT values around 1.8 at 600 K. A later experiment synthesized trigonal $TmAgTe_2$ and showed, although it has a very low thermal conductivity, that the highest ZT achieved is 0.35 due to the limited hole concentration. Carrete *et al.* combined the Boltzmann transport theory with constant mean free path approximation (CMFP) to study the thermoelectric properties of 75 nanograined HHs.[18] Five candidates were identified for room and high temperature applications, respectively. Xi *et al.* combined the Boltzmann transport theory with constant electron–phonon coupling approximation (CEPC) to calculate the electrical transport properties of 161 p-type diamond-like chalcogenides.[19] They found that vacancy-containing chalcogenides, such as $CdIn_2Te_4$ and $ZnIn_2Te_4$, could have high thermoelectric performance. One of the variations, $Cd_2Cu_3In_3Te_8$, was synthesized and showed that ZT values are above

Skolkovo Institute of Science and Technology, Bolshoy Boulevard 30, bld. 1, 121205 Moscow, Russia. E-mail: Tao.Fan@skoltech.ru

† Electronic supplementary information (ESI) available. See DOI: 10.1039/d1tc03146e

1 at high temperatures. Besides these works which calculated thermoelectric properties directly under various approximations, there are also other works based on semi-empirical models to screen the materials.[20–24] For example, Toberer *et al.* proposed a semi-empirical descriptor β_{SE} to quantify a materials potential for high *ZT* when appropriately doped.[20] β_{SE} is composed of room temperature intrinsic charge carrier mobility μ_0 and lattice thermal conductivity κ_L, and both of them can be computed by semi-empirical models. Their tests showed that good thermoelectric materials are correctly identified as ones with large values of β_{SE}. Using this descriptor, these authors studied the thermoelectric properties of 518 binary A1B1 compounds and 427 binary quasi-2D compounds successively, and found many promising candidates that have not been previously considered.[21,22] Jia *et al.* proposed two descriptors – the electrical descriptor χ and the lattice anharmonicity descriptor γ – in order to characterize the power factor and lattice thermal conductivity, respectively.[24] χ can be calculated using the deformation potential theory and the rigid band approximation, while γ can be evaluated based on the variation of the elastic properties with the volume. The authors screened 243 binary semiconductor chalcogenides in the database using the two descriptors. 50 compounds were identified as promising thermoelectric materials with both good electronic properties and low thermal conductivities. Among them, 9 p-type and 14 n-type materials were new. Although the methods mentioned above have been widely used and led to many discoveries, there are some problems within these methods. For example, both CRTA and CMFP assume the electronic relaxation time is energy independent and has the same constant value for different materials. The accuracy of such assumptions has always been questioned. However, an accurate calculation of the relaxation time by a fully *ab initio* method is very time-consuming and is not suitable for high-throughput calculations. Moreover, in all of these high-throughput works, lattice thermal conductivity is either taken from experiments on already known materials or calculated by simple models.

Chalcogenides have been under the limelight in the field of thermoelectricity, because most of the high performance thermoelectric materials belong to chalcogenides or their alloys.[25–27] Still, this group of materials are not being explored fully. In this work, we employed a program developed by our group, AICON2 (*Ab Initio* CONductivities, version 2),[28] to study the thermoelectric transport properties of 127 cubic chalcogenides. There are two highlights of our methods: first, beyond the CRTA, the energy and temperature dependent electronic relaxation time was calculated with an efficient algorithm. Therefore, transport parameters, such as electrical conductivity, can be directly obtained without predefining relaxation time. Second, lattice thermal conductivity was calculated by a modified Debye–Callaway model, which is quite accurate for a wide range of materials at room temperature and above.[28,29] The power factor results show 46 potential candidates for thermoelectricity, including 5 already well-known thermoelectric compounds. Furthermore, after adding lattice thermal conductivity and computing the figure of merit, we found 19 novel materials could have *ZT* values larger than 1 in the temperature range of 300–1000 K if doped appropriately, for either n-type or p-type.

2 Methods

2.1 Electrical transport properties

Electrical transport properties can be calculated based on the generalized Kane band model and perturbation theory in the framework of the relaxation time approximation (RTA).[30,31] Assuming the material is homogeneous and the relaxation time τ is independent of the direction of the crystal momentum **k** when the external field is weak, all the transport coefficients can be expressed in terms of an averaged quantity, namely $\langle \tau^l z^q \rangle$:[28]

$$\langle \tau^l z^q \rangle = \frac{\int_0^\infty \left(-\frac{\partial f}{\partial z}\right) \left[\frac{\tau(z)}{m_d^*(z)}\right]^l z^q k^3 \mathrm{d}z}{\int_0^\infty \left(-\frac{\partial f}{\partial z}\right) \frac{k^3}{m_{d_0}^{*l}} \mathrm{d}z} \quad (1)$$

where $f = 1/(e^{(\varepsilon-\eta)/k_BT} + 1)$ is the Fermi–Dirac distribution function; $z = \varepsilon/k_BT$ is the reduced band energy, k_B is the Boltzmann constant; $m_{d_0}^*$ is the density of states (DOS) effective mass at the band edge, while m_d^* is the DOS effective mass at energy z; l and q are constants. The parameters τ, k, and m_d^* can all be expressed as a function of z. All thermoelectric related properties, including carrier mobility μ, carrier concentration n, electrical conductivity σ, Seebeck coefficient α, and electronic thermal conductivity κ_e can be expressed as:

$$\mu = \frac{e\langle\tau\rangle}{m_c^*} \quad (2)$$

$$n = \frac{(2m_{d_0}^* k_B T)^{3/2}}{3\pi^2\hbar^3} \int_0^\infty \left(-\frac{\partial f}{\partial z}\right)(z + \beta z^2)^{3/2} \mathrm{d}z \quad (3)$$

$$\sigma = ne\mu \quad (4)$$

$$\alpha = \frac{k_B}{e} \frac{\langle \tau(z-\zeta) \rangle}{\langle \tau \rangle} \quad (5)$$

$$L_0 = \left(\frac{k_B}{e}\right)^2 \left\{ \frac{\langle \tau z^2 \rangle}{\langle \tau \rangle} - \left[\frac{\langle \tau z \rangle}{\langle \tau \rangle}\right]^2 \right\} \quad (6)$$

$$\kappa_e = L_0 T \sigma \quad (7)$$

where e is the elementary charge and $\hbar$ is the Planck constant; $\zeta = \eta/k_BT$ is the reduced chemical potential; $\beta = k_BT/\varepsilon_g$; m_c^* is the conductivity effective mass.

2.1.1 Kane band model. A generalized Kane band model is used to account for the nonparabolicity of the energy band with respect to crystal momentum **k**. In the Kane band model, it is assumed that the constant energy surface for any energy value is ellipsoidal and the effective mass of carriers (both electrons

and holes) is determined by the interaction of the lowest conduction band with the highest valence band. The relation between the energy and crystal momentum is expressed as[31]

$$\frac{\hbar^2 k_\perp{}^2}{m^*_{\perp 0}} + \frac{\hbar^2 k_\parallel{}^2}{2m^*_{\parallel 0}} = \varepsilon\left(1 + \frac{\varepsilon}{\varepsilon_g}\right) \tag{8}$$

here ε_g is the band gap; $k_\perp$ and $k_\parallel$ are the transverse and longitudinal components of the momentum **k**; $m^*_{\perp 0}$ and $m^*_{\parallel 0}$ are the transverse and longitudinal components of the effective mass tensor at the band edge. The part in parentheses indicates the nonparabolicity of the band. The DOS effective mass is expressed as

$$m^*_d = N^{2/3} m^*_b = N^{2/3}(m^*_\parallel m^{*2}_\perp)^{1/3} \tag{9}$$

here N is the degeneracy of the band due to the symmetry. The effective mass can be calculated from first-principles, then the value of the momentum k can be defined as

$$k(z) = \frac{(2k_B T m^*_{b_0})^{1/2}}{\hbar}[z(1+\beta z)]^{1/2} \tag{10}$$

and the density of states is

$$\rho(z) = \frac{(2k_B T)^{1/2} m^{*3/2}_{d_0}}{\pi^2 \hbar^3}[z(1+\beta z)]^{1/2}(1+2\beta z) \tag{11}$$

2.1.2 Relaxation time of different scattering mechanisms.

As seen in eqn (1), the key variable for calculating transport coefficients is τ. In order to calculate τ, three scattering mechanisms – acoustic phonon scattering, polar optical phonon scattering, and ionized impurities scattering – are considered here, with corresponding relaxation times τ_{aco}, τ_{opt}, and τ_{imp}. The total relaxation time is the sum of these relaxation times according to Matthiessens rule:

$$\frac{1}{\tau} = \frac{1}{\tau_{aco}} + \frac{1}{\tau_{opt}} + \frac{1}{\tau_{imp}} \tag{12}$$

The strength of the acoustic phonon scattering can be represented by the deformation potential constants. The main expression for this kind of scattering, originally proposed by Bardeen for calculating the mobility of nonpolar isotropic semiconductors, is widely used.[32] Ravich added the effect of band nonparabolicity as well as the dependence of the matrix element of the interaction of carriers with the acoustic phonons on the energy in the nonparabolic region. The formula is given by[31]

$$\frac{1}{\tau_{aco}(z)} = \frac{\pi k_B T \rho \Xi^2}{\hbar c N}\left[1 - \frac{8\beta(z+\beta z^2)}{3(1+2\beta z)^2}\right] \tag{13}$$

where Ξ is the deformation potential constant; c is the elastic constant related to longitudinal and transverse acoustic wave velocity. The factor in brackets describes the energy dependence of the squared matrix element of the electron–phonon interaction.

In a polar crystal, the polar scattering by the long-wavelength longitudinal optical phonons gives rise to approximately the same temperature dependence as the acoustic phonon scattering at some temperatures. The polar scattering is strongly inelastic at low temperatures. However, it can be regarded as almost elastic above the compounds Debye temperature, and the relaxation time concept can be used. Moreover, since the density of free carriers in real applications is always high, it screens the electric field produced by optical vibrations in polar crystals. This screening effect reduces the strength of the polar scattering and should also be included. The formula for the polar scattering is[31]

$$\frac{1}{\tau_{opt}(z)} = \frac{2^{1/2} k_B T e^2 m^{*1/2}_{b_0}(\varepsilon_\infty{}^{-1} - \varepsilon_0{}^{-1})}{\hbar^2 (z k_B T)^{1/2}} \frac{1+2\beta z}{(1+\beta z)^{1/2}} \times \left\{\left[1 - \delta \ln\left(1+\frac{1}{\delta}\right)\right] - \frac{2\beta(z+\beta z^2)}{(1+2\beta z)^2} \times \left[1 - 2\delta + 2\delta^2 \ln\left(1+\frac{1}{\delta}\right)\right]\right\} \tag{14}$$

where ε_∞ and ε_0 are the high-frequency and static dielectric constants; $\delta = (2k r_\infty)^{-2}$ with the screening radius r_∞ of the medium with ε_∞:

$$r_\infty{}^{-2} = \frac{4\pi e^2 \rho(z)}{\varepsilon_\infty} \tag{15}$$

Scattering by ionized impurities and vacancies is the dominant mechanism at very low (liquid helium) temperatures in highly degenerate samples. It is described by the formula[30]

$$\frac{1}{\tau_{imp}(\zeta)} = \frac{2e^4 N m^*_{b_0}(1+2\beta\zeta)\Phi(\delta_0)}{3\pi\varepsilon_0{}^2\hbar^3} \tag{16}$$

where $\Phi(\delta_0)$ is the logarithmic factor:

$$\Phi(\delta_0) = \ln(1 + \delta_0{}^{-1}) - (1+\delta_0)^{-1} \tag{17}$$

with $\delta_0 = (2k r_0)^{-2}$ and r_0 is the screening radius of a medium with dielectric constant ε_0. In highly degenerate samples

$$r_0{}^{-2} = \frac{4\pi e^2 \rho(\zeta)}{\varepsilon_0} \tag{18}$$

The above formulas have been implemented in our program AICON2. See ref. 28 for a detailed explanation of the model and computational procedures.

2.2 Lattice thermal conductivity

Lattice thermal conductivity was calculated by a modified Debye–Callaway model, which is also implemented in our code AICON2. The original Debye–Callaway model only considers acoustic phonons contribution, while in our modified model, we also account for the contribution from optical phonons. The formulas for lattice thermal conductivity are as follows:

$$\kappa = \kappa_{LA} + \kappa_{TA} + \kappa_{TA'} + \kappa_O \tag{19a}$$

$$\kappa_i = \kappa_{i1} + \kappa_{i2}\ (i = \mathrm{TA}, \mathrm{TA}', \mathrm{LA}) \tag{19b}$$

$$\kappa_{i1} = \frac{1}{3} C_i T^3 \int_0^{\theta_i/T} \frac{\tau^i_C(x) x^4 e^x}{(e^x - 1)^2} \mathrm{d}x \tag{19c}$$

$$\kappa_{i2} = \frac{1}{3} C_i T^3 \frac{\left[\int_0^{\theta_i/T} \frac{\tau_C^i(x) x^4 e^x}{\tau_N^i(x)(e^x-1)^2} \mathrm{d}x\right]^2}{\int_0^{\theta_i/T} \frac{\tau_C^i(x) x^4 e^x}{\tau_N^i(x)\tau_R^i(x)(e^x-1)^2} \mathrm{d}x} \quad (19d)$$

$$\kappa_O = \frac{1}{3}(3p-3)\frac{N}{V} k_B f_E \left(\frac{\Theta_E}{T}\right) \nu_O^2 \tau_C^O \left[1 + \frac{\tau_R^O}{\tau_N^O}\right] \quad (19e)$$

In these expressions, θ_i is the Debye temperature for each phonon branch, $C_i = {k_B}^4/(2\pi^2\hbar^3\nu_i)$ and $x = \hbar\omega/k_BT$, where ω is the phonon frequency, and ν_i is the phonon velocity for each branch. p is the number of atoms in the primitive cell; thus, $3p - 3$ is the number of optical branches. N is the number of primitive cells (usually, $N = 1$), V is the volume of the primitive cell. The function f_E is the Einstein function. τ_N^i is the relaxation time of the normal phonon process, τ_R^i is the total relaxation time of all the resistive scattering processes, which includes phonon–phonon Umklapp scattering and isotope point defect scattering $(\tau_R^i)^{-1} = (\tau_U^i)^{-1} + (\tau_I^i)^{-1}$. Finally, $(\tau_C^i)^{-1} = (\tau_N^i)^{-1} + (\tau_R^i)^{-1}$. The main difficulty of using the above formulas to calculate lattice thermal conductivity is how to get those relaxation times of different phonon branches. This would require an account of anharmonicity, with at least third-order force constants and three-phonon processes. In our model, we use a much simpler way to calculate these relaxation times as proposed by Morelli.[33] Take the Umklapp scattering rate $(\tau_U^i)^{-1}$ as an example. The phonon–phonon Umklapp processes dominate at high temperatures, following an exponential behaviour

$$[\tau_U^i(x)]^{-1} = B_U^i \left(\frac{k_B}{\hbar}\right)^2 x^2 T^3 \mathrm{e}^{-\theta_i/3T} \quad (20a)$$

where

$$B_U^i = \frac{\hbar {\gamma_i}^2}{M \nu_i^2 \theta_i} \quad (20b)$$

The Umklapp scattering rate thus depends on the characteristic Debye temperature, phonon velocity, and Grüneisen parameter of each branch. All these quantities can be easily obtained by first-principles calculations. The detailed description and the way to calculate these parameters can be found in ref. 28 and 29.

2.3 First-principles calculations

All density functional theory (DFT) calculations were performed using the Vienna *Ab initio* Simulation Package (VASP) with the Perdew–Burke–Ernzerhof generalized gradient approximation (PBE-GGA) and the projector augmented wave (PAW) potentials.[34–36] For structure relaxation, the plane wave kinetic energy cutoff was set to 600 eV and the Brillouin zone was sampled using Γ-centered meshes with the reciprocal-space resolution of $2\pi \times 0.03$ Å^{-1}. Kohn–Sham equations were solved self-consistently with a total energy tolerance of 10^{-7} eV per cell and structures were relaxed until the maximum force became smaller than 10^{-3} eV Å^{-1}. The dielectric constants were calculated using density-functional perturbation theory,[37] and the elastic constants were calculated using the finite difference method as implemented in VASP. To get the deformation potential constants of a compound, three band structure calculations were run: one at the equilibrium volume, the other two at volumes larger by 0.1% and 0.2%. For compounds containing heavy atoms ($Z > 80$), the spin–orbit coupling (SOC) effect was included in all band related calculations.

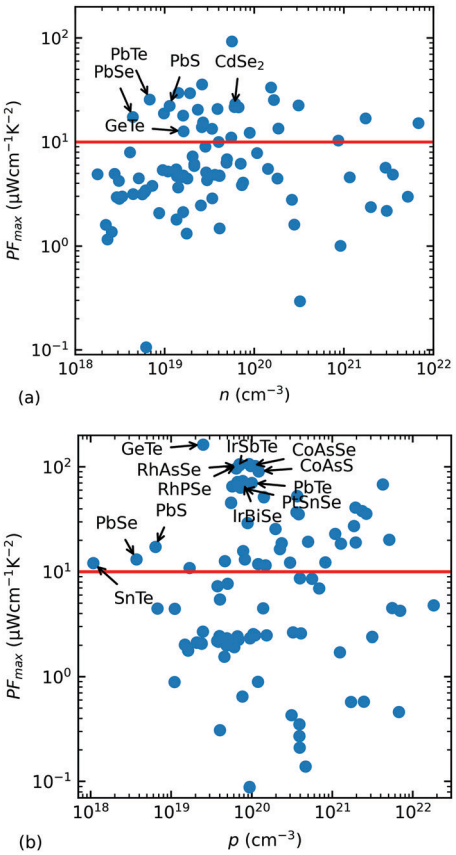

Fig. 1 Maximum power factor as a function of the corresponding carrier concentration for the studied compounds in the temperature range of 300 K to 1000 K, n-type (a) and p-type (b). Some compounds with high power factor are marked.

Phonon related properties, including phonon frequency, phonon velocity and Grüneisen parameter, were calculated using the Phonopy package[38] combined with VASP. The forces were calculated for a minimal set of supercells with atomic displacements generated by Phonopy, and then collected to get second-order interatomic force constants (IFCs). In order to calculate Grüneisen parameters, three phonon calculations have to be run: one at the equilibrium volume, and the other two at slightly smaller (−0.4%) and larger volume (+0.4%).

To enable high-throughput screening, the automated workflow control for structural relaxations, electronic and phonon structures, and transport properties has been developed and implemented in our program AICON2 based on Materials Project high-throughput infrastructure.[39–41]

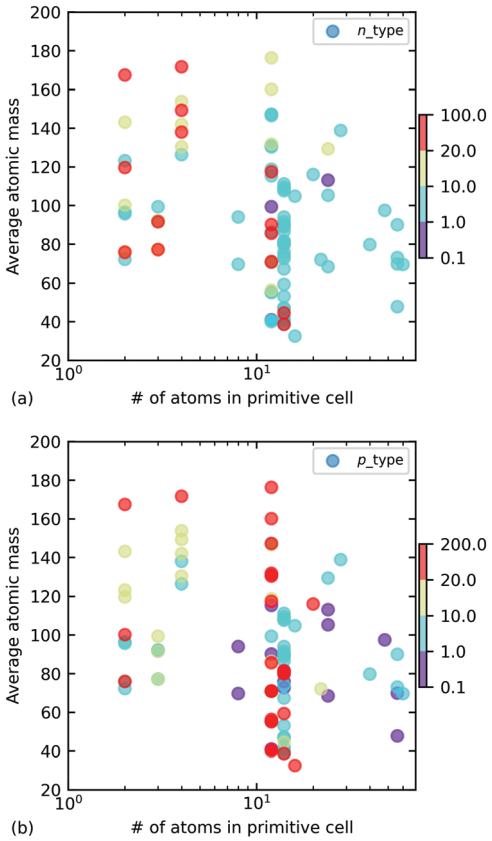

Fig. 2 Maximum power factor values of the studied compounds in the chemical space composed by average atomic mass and number of atoms in the primitive cell, represented by the color for n-type and p-type transport. The unit is μW cm^{-1} K^{-2}.

3 Results and discussion

All structures were extracted from the Materials Project database[42] with five searching criteria: (1) S, Se and Te as anions; (2) the band gap should be larger than 0 eV but smaller than 1.2 eV, since good thermoelectric materials are usually narrow gap semiconductors; (3) the energy above the convex hull line should be less than 0.1 eV per atom to ensure the structure is thermodynamically stable or at least potentially synthesizable in experimental conditions; (4) cubic symmetry (in later works, we shall explore lower symmetries too); (5) non-ferromagnetic phase, since the band structures of the ferromagnetic phases need special consideration within DFT and are thus unsuitable for an automatic approach such as the present. These criteria resulted in 127 entries out of the database. Then, automatic calculations for these structures were carried out. Since GGA is known to underestimate the band gap, the calculated band gaps of some structures with very small gap could be zero. These structures were just discarded. Finally, 94 compounds have finished the complete processes of the electrical transport properties calculation. Among these compounds, 46 compounds have a maximum power factor greater than 10 μW cm^{-1} K^{-2} in the temperature range from 300 K to 1000 K. These compounds were used further to calculate their lattice thermal conductivity and figure of merit.

Fig. 1 shows the maximum power factor with respect to the carrier concentration reaching this maximum value for both n- and p-type. Five compounds, PbTe, PbS, PbSe, GeTe, and SnTe, are already well-known thermoelectric materials and have high power factor values according to our calculation, which validates our methods. There is one important issue that needs to be mentioned here. As explained in the last section, only those compounds containing heavy elements ($Z > 80$) include SOC in their band structure calculations. One could include SOC also for compounds with lighter elements (*e.g.*, GeTe and SnTe), but such calculations will be more expensive and unnecessary for the kind of screening we do. For the above mentioned examples of GeTe and SnTe, our screening without SOC correctly identifies these compounds as good thermoelectric materials.

Table 1 Compounds with calculated maximum *ZT* values greater than 1 in temperature range 300–1000 K. The entry id corresponds to its Materials ID in the Materials Project

Formula	Entry id	Doping type	PF_{max} (μW cm^{-1} K^{-2})	ZT_{max}
CoAsS	mp-16363	p-Type	90.58	1.14
CoAsSe	mp-1226036	p-Type	101.91	1.25
PtSnSe	mp-1218926	p-Type	63.22	1.51
RhAsSe	mp-1228724	p-Type	103.27	1.13
RhPSe	mp-1102531	p-Type	105.54	1.21
IrBiSe	mp-1103228	p-Type	73.27	1.18
IrSbTe	mp-1102430	p-Type	96.18	1.43
$CdSe_2$	mp-1095493	n-Type	21.77	1.35
$KAcTe_2$	mp-863710	n-, p-type	11.05(n), 12.61(p)	2.17(n), 2.24(p)
$RbAcTe_2$	mp-862797	n-, p-type	13.51(n), 13.11(p)	2.93(n), 2.72(p)
$CsAcTe_2$	mp-867341	n-, p-type	10.35(n), 12.22(p)	2.84(n), 3.07(p)
$GaAcTe_2$	mp-861884	n-, p-type	29.58(n), 7.68(p)	6.99(n), 3.05(p)
$InAcTe_2$	mp-867112	n-, p-type	29.83(n), 10.89(p)	2.99(n), 1.67(p)
$TlAcTe_2$	mp-865028	n-, p-Type	36.01(n), 23.03(p)	4.27(n), 3.26(p)
$Hg_2Al_4Se_8$	mp-1103510	p-Type	67.72	1.63
$Cd_2In_4Se_4S_4$	mp-1226914	p-Type	27.29	1.12
$Hg_2In_4S_8$	mp-22356	p-Type	41.04	1.30
$Nb_6Sb_4Te_{10}$	mp-569571	p-Type	37.13	1.11
MgTe	mp-1008786	p-Type	52.55	1.32

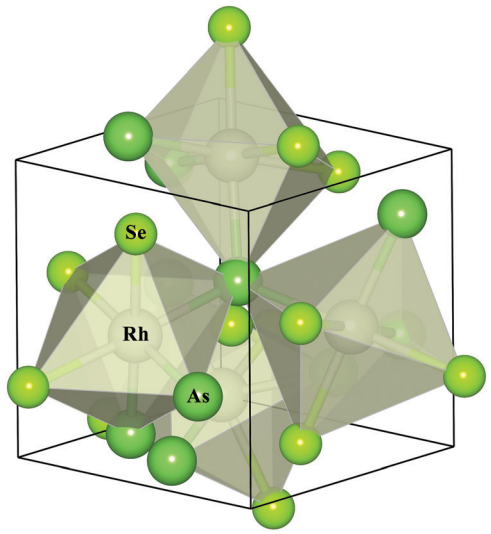

Fig. 3 Crystal structure of RhAsSe.

The power factor results can also be rendered from another format. In Fig. 2, materials are presented according to their average atomic mass and the number of atoms in the primitive cell. Materials with high power factor are found all across this chemical space, showing quite a high diversity.

Table 1 lists 19 novel compounds we found that have maximum ZT values larger than 1 within the temperature range of 300–1000 K. Next, we will introduce the most promising compounds for n-type and p-type, respectively. The results of other compounds can be found in the ESI.†

3.1 $X_4Y_4Z_4$ (X = VIII B, Y = IV A, V A, Z = VI A)

Compounds with this chemical formula, including RhAsSe, RhSbTe, IrSbTe, IrBiSe, IrBiTe, RhBiSe, RhBiTe, CoAsS, CoAsSe, CoPS, CoPSe, RhPSe, CoSbS, PtSnSe, and PtGeTe, are found to be good p-type thermoelectric materials due to their high power factor. These compounds share the same structure (space group $P2_13$) and they belong to the pyrite structure type, as shown in Fig. 3. The transition metal X atoms are bonded to six Y and Z atoms, forming a distorted octahedron, while the Y (Z) atoms are tetrahedral, being bound to three X atoms and one other Z (Y) atom.

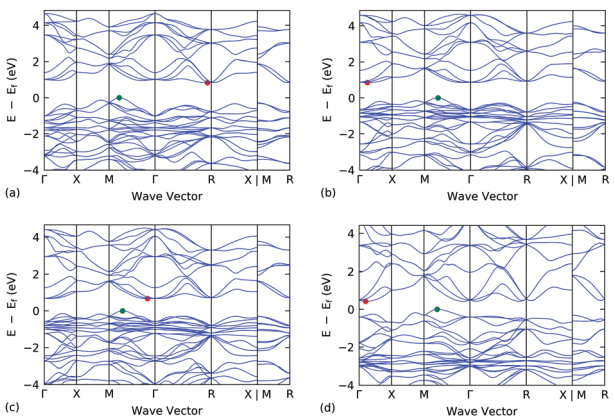

Fig. 4 Band structures of (a) RhAsSe, (b) CoAsS, (c) CoAsSe, and (d) PtSnSe. The CBM and VBM are shown by red and green points, respectively.

Table 2 Conductivity effective mass m_c^* and density of states effective mass m_d^* at the VBM of the studied compounds

	m_c^*/m_e	m_d^*/m_e
CoAsS	0.5128	2.8524
CoAsSe	0.4413	2.4915
CoPS	0.4862	2.7459
CoPSe	0.4349	2.4668
CoSbS	0.5315	2.9145
RhPSe	0.3805	2.1787
RhAsSe	0.3712	2.0853
RhBiSe	0.3545	1.9159
RhBiTe	0.2798	1.5197
RhSbTe	0.2929	1.6533
IrBiSe	0.3601	1.9450
IrBiTe	0.3152	1.7895
IrSbTe	0.3045	1.8577
PtSnSe	0.3206	1.9248
PtGeTe	0.2307	1.4327

Fig. 4 shows the band structures of these compounds, taking RhAsSe, CoAsS, CoAsSe, and PtSnSe as examples (others can be found in the ESI†). They are all indirect gap semiconductors. Their CBMs are located along the Γ–R or Γ–M or Γ–X path. However, the energy difference among these conduction bands is quite small, and they are probably all involved in electronic transport. Moreover, the CBMs of these compounds are quite flat, implying large effective masses. On the contrary, their VBMs are well-defined and located along the Γ–M path. Besides, the VBMs are dispersive and the corresponding effective masses are expected to be small. It is known that the Seebeck coefficient is proportional to the density of states effective mass m_d^*. According to eqn (9), there are two ways to improve the Seebeck coefficient: either increase N or increase $m_\parallel^* m_\perp^{*2}$. However, increasing the latter will also lead to larger conductivity effective mass m_c^*, defined as $3/m_c^* = \left(1/m_\parallel^* + 2/m_\perp^*\right)$; thus, small mobility and electrical conductivity. The merit of RhAsSe and other compounds belonging to this group is that the degeneracy of points along the Γ–M path is large ($N = 12$). Therefore, for p-type conduction, these compounds have large DOS effective mass, but reserve small conductivity effective mass (see Table 2). This will lead to large power factor values.

In order to explore the origin of the high band degeneracy and low band effective mass of VBMs of these compounds, we also calculate atomic- and orbital-projected band structures for these compounds using LOBSTER with the pbeVaspFit2015 basis set.[43–45] See the ESI† for the projected band results. Taking CoAsS as an example (Fig. S1, ESI†), its VBM includes contributions from all three types of atoms. Checking the orbital-projected band structure, it is mainly made of the Co 3d and 4p orbitals, As 4p orbital and S 3p orbital. The variation of effective mass of VBM for these compounds could be partly explained by the amount of contribution from these orbitals.

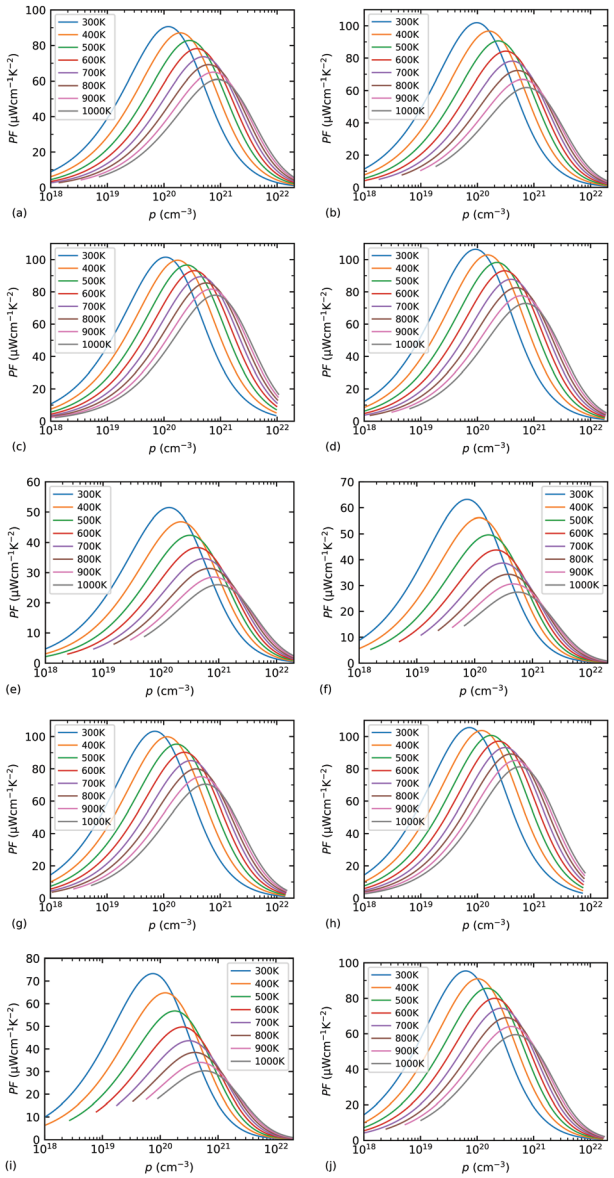

Fig. 5 Power factors at varying temperatures and carrier concentrations for (a) CoAsS, (b) CoAsSe, (c) CoPS, (d) CoPSe, (e) CoSbS, (f) PtSnSe, (g) RhAsSe, (h) RhPSe, (i) IrBiSe, and (j) IrSbTe.

For example, in the series CoPS–CoAsS–CoSbS, the effective mass increases as Table 2 shows. Comparing their orbital-projected band structure (Fig. S1b, S4b and S8b, ESI†), it is clear that the Co 3d orbital contribution increases while sulfur and Y type atom p orbital contributions decrease as the Y atom varies from P to Sb. Since d electrons are more localized than p electrons, the effective mass is supposed to be heavier.

Fig. 5 shows the power factor as a function of temperature and carrier concentration for some of these compounds, others can be found in the ESI.† The power factors of these compounds are extremely high in a wide temperature and carrier concentration range. The maximum values of some of them, such as CoAsSe, CoPS, CoPSe, RhPSe, and RhAsSe, could be even higher than 100 μW cm^{-1} K^{-2} according to our

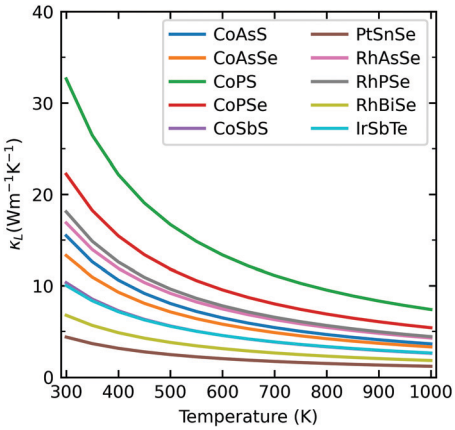

Fig. 6 Lattice thermal conductivity calculated by AICON2.

calculation. Just a reminder that the power factor values of the state-of-the-art thermoelectric materials, such as Bi_2Te_3 and PbTe, are usually 30–50 μW cm^{-1} K^{-2}. As explained above, such a large power factor is due to the special characteristics of their band structures: around VBM, they have large m_d^* due to the high degeneracy, but small m_c^* for each carrier pocket. Therefore, they could achieve both a high Seebeck coefficient and high electrical conductivity.

However, the problem with these compounds is that they also have high lattice thermal conductivity, as shown in Fig. 6. Due to this, the figure of merit values of these compounds are not much greater than those state-of-the-art thermoelectric materials (Fig. 7). However, some of them could still have figure of merit values above 1 at high temperatures, such as CoAsS, CoAsSe, PtSnSe, RhAsSe, RhPSe, IrBiSe, and IrSbTe. Furthermore, there are ways to reduce the lattice thermal conductivity of these compounds. For example, by alloying to form compounds like CoP(As,Sb)S(Se) that could reduce the lattice thermal conductivity efficiently while retaining the high power factor. Therefore, this group of compounds is quite promising for thermoelectric applications.

3.2 $CdSe_2$

The structure of $CdSe_2$ is shown in Fig. 8, the unit cell contains 12 atoms (4 Cd and 8 Se) and has a space group $Pa\bar{3}$. It also has a pyrite type structure. Cd atoms occupy the corner and face center of the unit cell and it forms an octahedron with six Se atoms around it. A different octahedron is connected by one Se atom. This compound is found to be a promising n-type thermoelectric material according to our calculation. Interestingly, we found an independent preprint also declares that this $CdSe_2$ is a good thermoelectric material.[46] We will compare our results with theirs below.

Fig. 9 shows the band structure of $CdSe_2$. Its VBM is located at the Γ point and CBM is along the Γ–R path. The CBM is dispersive and has a small conductivity effective mass $m_c^* = 0.41m_e$ ($0.43m_e$ from ref. 46). Meanwhile, the band degeneracy N of CBM is 8 and the density of states effective mass is $m_d^* = 1.64m_e$. Therefore, similar to the CoAsS-like compounds

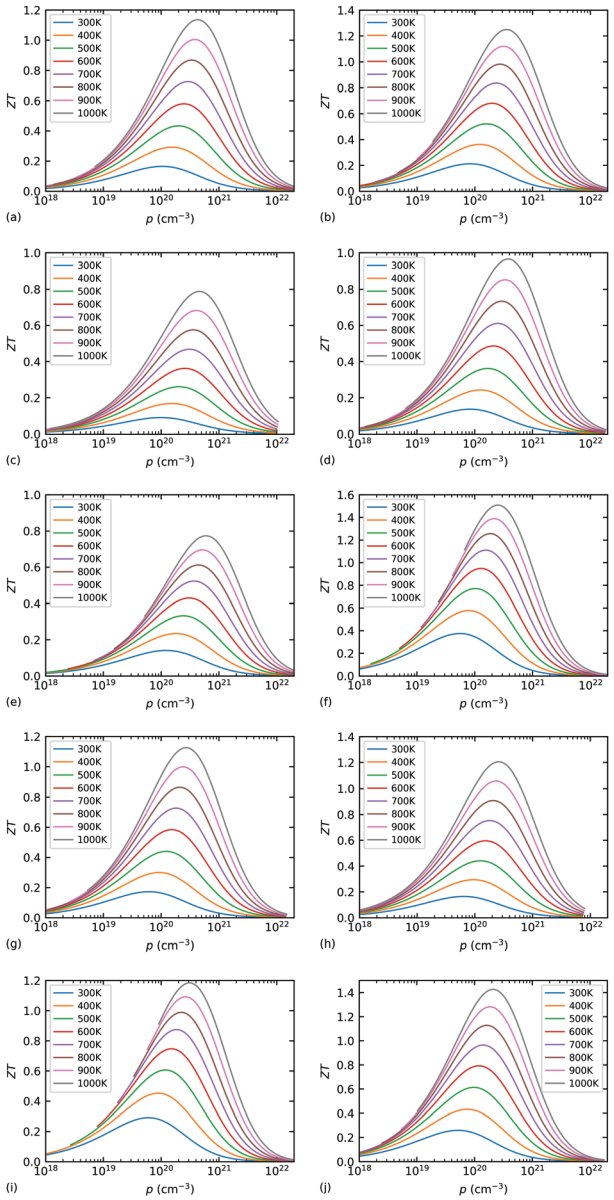

Fig. 7 Figure of merit at varying temperatures and carrier concentrations for (a) CoAsS, (b) CoAsSe, (c) CoPS, (d) CoPSe, (e) CoSbS, (f) PtSnSe, (g) RhAsSe, (h) RhPSe, (i) IrBiSe, and (j) IrSbTe.

discussed in the above section, $CdSe_2$ could also have both a high Seebeck coefficient and high electrical conductivity.

Fig. S32a and b (ESI†) shows the atomic- and orbital-projected band structure of $CdSe_2$. Both Cd and Se contribute to the formation of CBM. Specifically, it is mainly composed of a Cd 5s orbital and Se 4p orbital. Fig. 10 shows the calculated power factor, lattice thermal conductivity and figure of merit at different temperatures and carrier concentrations for n-type transport. The power factor is generally high in a wide temperature range (Fig. 10a). Meanwhile, the lattice thermal conductivity of $CdSe_2$ is low, especially at high temperatures (Fig. 10b). Therefore, the figure of merit could be larger than 1 at a high temperatures (Fig. 10c). Our figure of merit is generally in good agreement with the results from ref. 46.

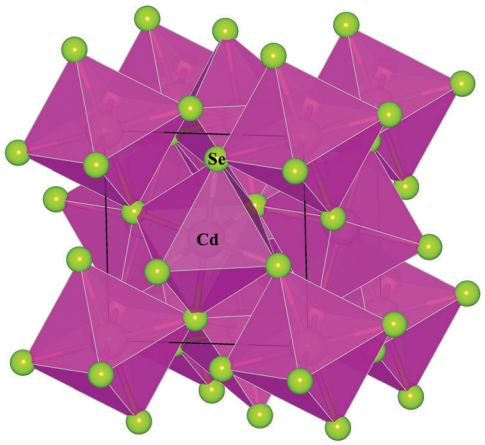

Fig. 8 Crystal structure of $CdSe_2$.

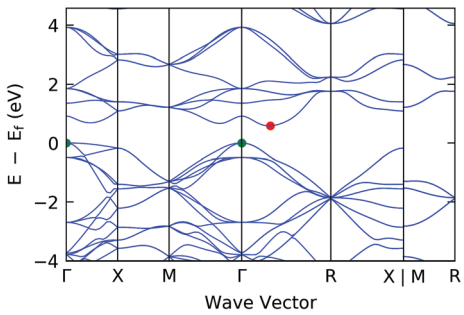

Fig. 9 Band structure of $CdSe_2$.

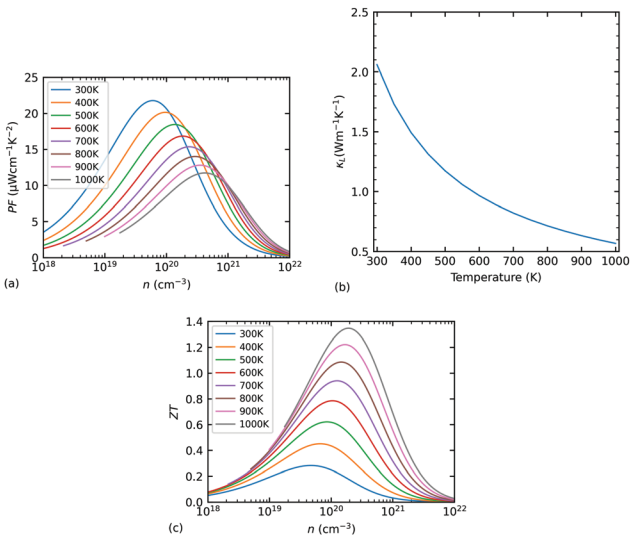

Fig. 10 Thermoelectric properties of $CdSe_2$ for n-type transport. (a) Power factor, (b) lattice thermal conductivity, and (c) figure of merit.

The maximum ZT value at 900 K is 1.22 at a concentration of 1.70×10^{20} cm^{-3} according to our calculations, while it is 1.16 at 1.91×10^{20} cm^{-3} according to ref. 46. However, our power factor and lattice thermal conductivity are higher than theirs.

For example, our maximum power factor is 21.77 μW cm^{-1} K^{-2} and lattice thermal conductivity is 2.06 W m^{-1} K^{-1} at 300 K, while their values are 9.7 μW cm^{-1} K^{-2} and 0.75 W m^{-1} K^{-1} at the same temperature. In the end, both studies independently prove that pyrite $CdSe_2$ has a high *ZT* and is a promising thermoelectric material.

4 Conclusions

In this work, we report a high-throughput screening for finding novel thermoelectric materials. Using software developed in our group, the thermoelectric related transport properties can be evaluated in a wide temperature and carrier concentration range without any predefined parameters. Meanwhile, with the help of advanced workflow management tools, the whole calculation process is fast. Among 127 cubic chalcogenide compounds extracted from the Materials Project, 46 compounds were identified as having a high power factor for either n-type or p-type transport, including five already well-known thermoelectric materials. Furthermore, the figure of merit *ZT* results suggest 19 compounds which have not been experimentally studied are potentially good thermoelectric materials. Especially, CoAsS and compounds belonging to this group have an extremely high power factor for p-type transport – the maximum power factor could even be larger than 100 μW cm^{-1} K^{-2}, far beyond that of any well-known thermoelectric materials. Because of the high power factor, some of these compounds, such as CoAsS, CoAsSe, PtSnSe, RhAsSe, RhPSe, IrBiSe, and IrSbTe, could have *ZT* values greater than 1 in the temperature range of 300–1000 K. Detailed analysis of their band structures shows that it is the high band degeneracy of VBM that causes such an excellent thermoelectric behavior. Due to the high band degeneracy, this group of materials could have both high Seebeck coefficient and high electrical conductivity. As for n-type thermoelectric materials, we found $CdSe_2$, which has a relatively high power factor and very low lattice thermal conductivity, to be a promising one. Experimental investigation on these compounds is strongly encouraged. Future work will also explore non-cubic chalcogenides. The methods used in this work could also be applied in other fields where transport properties of semiconductors are needed.

Author contributions

T. F. initiated the project, performed the calculations, analysed the data, and wrote the manuscript. A. R. O. participated in discussions of the method and results and revised the manuscript.

Conflicts of interest

There are no conflicts to declare.

Acknowledgements

We acknowledge the usage of the Skoltech HPC cluster ARKUDA for obtaining the results presented in this paper. This work is funded by the Russian Science Foundation (grant 19-72-30043).

Notes and references

1 D. M. Rowe, *Thermoelectrics handbook: macro to nano*, CRC Press, 2018.
2 G. Tan, L. Zhao and M. G. Kanatzidis, *Chem. Rev.*, 2016, **116**, 12123–12149.
3 X. Shi, L. Chen and C. Uher, *Int. Mater. Rev.*, 2016, **61**, 379–415.
4 G. Tan, M. Ohta and M. G. Kanatzidis, *Philos. Trans. R. Soc., A*, 2019, **377**, 20180450.
5 L. E. Bell, *Science*, 2008, **321**, 1457–1461.
6 J. G. Snyder, E. S. Toberer, R. Khanna and W. Seifert, *Phys. Rev. B: Condens. Matter Mater. Phys.*, 2012, **86**, 045202.
7 Y. Pei, H. Wang and J. G. Snyder, *Adv. Mater.*, 2012, **24**, 6125–6135.
8 L. Zhao, S. Hao, S.-H. Lo, C.-I. Wu, X. Zhou, Y. Lee, H. Li, K. Biswas, T. P. Hogan and C. Uher, *et al.*, *J. Am. Chem. Soc.*, 2013, **135**, 7364–7370.
9 T. Zhu, Y. Liu, C. Fu, J. P. Heremans, J. G. Snyder and X. Zhao, *Adv. Mater.*, 2017, **29**, 1605884.
10 P. Gorai, V. Stevanović and E. S. Toberer, *Nat. Rev. Mater.*, 2017, **2**, 1–16.
11 S. Hao, V. P. Dravid, M. G. Kanatzidis and C. Wolverton, *npj Comput. Mater.*, 2019, **5**, 1–10.
12 J. J. G. Moreno, J. Cao, M. Fronzi and M. H. N. Assadi, *Mater. Renew. Sustain. Energy*, 2020, **9**, 1–22.
13 G. K. Madsen and D. J. Singh, *Comput. Phys. Commun.*, 2006, **175**, 67–71.
14 G. K. Madsen, *J. Am. Chem. Soc.*, 2006, **128**, 12140–12146.
15 J. Yang, H. Li, T. Wu, W. Zhang, L. Chen and J. Yang, *Adv. Funct. Mater.*, 2008, **18**, 2880–2888.
16 H. Zhu, G. Hautier, U. Aydemir, Z. M. Gibbs, G. Li, S. Bajaj, J.-H. Pöhls, D. Broberg, W. Chen and A. Jain, *et al.*, *J. Mater. Chem. C*, 2015, **3**, 10554–10565.
17 F. Ricci, W. Chen, U. Aydemir, G. J. Snyder, G.-M. Rignanese, A. Jain and G. Hautier, *Sci. Data*, 2017, **4**, 1–13.
18 J. Carrete, N. Mingo, S. Wang and S. Curtarolo, *Adv. Funct. Mater.*, 2014, **24**, 7427–7432.
19 L. Xi, S. Pan, X. Li, Y. Xu, J. Ni, X. Sun, J. Yang, J. Luo, J. Xi and W. Zhu, *et al.*, *J. Am. Chem. Soc.*, 2018, **140**, 10785–10793.
20 J. Yan, P. Gorai, B. Ortiz, S. Miller, S. A. Barnett, T. Mason, V. Stevanović and E. S. Toberer, *Energy Environ. Sci.*, 2015, **8**, 983–994.
21 P. Gorai, P. Parilla, E. S. Toberer and V. Stevanovic, *Chem. Mater.*, 2015, **27**, 6213–6221.
22 P. Gorai, E. S. Toberer and V. Stevanović, *J. Mater. Chem. A*, 2016, **4**, 11110–11116.

23 Z. Feng, Y. Fu, A. Putatunda, Y. Zhang and D. J. Singh, *Phys. Rev. B*, 2019, **100**, 085202.
24 T. Jia, Z. Feng, S. Guo, X. Zhang and Y. Zhang, *ACS Appl. Mater. Interfaces*, 2020, **12**, 11852–11864.
25 C. Han, Q. Sun, Z. Li and S. Dou, *Adv. Energy Mater.*, 2016, **6**, 1600498.
26 W. He, D. Wang, H. Wu, Y. Xiao, Y. Zhang, D. He, Y. Feng, Y. Hao, J. Dong and R. Chetty, *et al.*, *Science*, 2019, **365**, 1418–1424.
27 W. Liu, L. Yang, Z. Chen and J. Zou, *Adv. Mater.*, 2020, **32**, 1905703.
28 T. Fan and A. R. Oganov, *Comput. Phys. Commun.*, 2021, 108027.
29 T. Fan and A. R. Oganov, *Comput. Phys. Commun.*, 2020, **251**, 107074.
30 Y. I. Ravich, B. Efimova and V. Tamarchenko, *Phys. Status Solidi B*, 1971, **43**, 11–33.
31 I. I. Ravich, *Semiconducting lead chalcogenides*, Springer Science & Business Media, 2013, vol. 5.
32 J. Bardeen and W. Shockley, *Phys. Rev.*, 1950, **80**, 72.
33 D. Morelli, J. Heremans and G. Slack, *Phys. Rev. B: Condens. Matter Mater. Phys.*, 2002, **66**, 195304.
34 G. Kresse and J. Furthmüller, *Phys. Rev. B: Condens. Matter Mater. Phys.*, 1996, **54**, 11169.
35 G. Kresse and J. Furthmüller, *Comput. Mater. Sci.*, 1996, **6**, 15–50.
36 J. P. Perdew, K. Burke and M. Ernzerhof, *Phys. Rev. Lett.*, 1996, **77**, 3865.
37 X. Gonze and C. Lee, *Phys. Rev. B: Condens. Matter Mater. Phys.*, 1997, **55**, 10355.
38 A. Togo and I. Tanaka, *Scr. Mater.*, 2015, **108**, 1–5.
39 K. Mathew, J. H. Montoya, A. Faghaninia, S. Dwarakanath, M. Aykol, H. Tang, I.-H. Chu, T. Smidt, B. Bocklund and M. Horton, *et al.*, *Comput. Mater. Sci.*, 2017, **139**, 140–152.
40 A. Jain, S. P. Ong, W. Chen, B. Medasani, X. Qu, M. Kocher, M. Brafman, G. Petretto, G.-M. Rignanese and G. Hautier, *et al.*, *Concurr. Comput. Pract. Exp.*, 2015, **27**, 5037–5059.
41 S. P. Ong, W. D. Richards, A. Jain, G. Hautier, M. Kocher, S. Cholia, D. Gunter, V. L. Chevrier, K. A. Persson and G. Ceder, *Comput. Mater. Sci.*, 2013, **68**, 314–319.
42 A. Jain, S. P. Ong, G. Hautier, W. Chen, W. D. Richards, S. Dacek, S. Cholia, D. Gunter, D. Skinner and G. Ceder, *et al.*, *APL Mater.*, 2013, **1**, 011002.
43 S. Maintz, V. L. Deringer, A. L. Tchougréeff and R. Dronskowski, *J. Comput. Chem.*, 2013, **34**, 2557–2567.
44 S. Maintz, V. L. Deringer, A. L. Tchougréeff and R. Dronskowski, *J. Comput. Chem.*, 2016, **37**, 1030–1035.
45 R. Nelson, C. Ertural, J. George, V. L. Deringer, G. Hautier and R. Dronskowski, *J. Comput. Chem.*, 2020, **41**, 1931–1940.
46 T. Jia, J. Carrete, Y. Zhang and G. K. Madsen, 2020, arXiv preprint arXiv:2005.05916.